

## CT-Based Attenuation Correction on the FLEX Triumph Preclinical PET/CT Scanner

PRASAD, Rameshwar, *et al.*

### Abstract

Generation of accurate attenuation maps is crucial for reliable attenuation correction of PET data and hence is a prerequisite for accurate quantification of biological processes. In this study, we implemented the CTAC procedure on the FLEX Triumph™ preclinical PET/CT scanner and evaluated tube voltage dependence for different kVps (40, 50, 60, 70, and 80). The quantitative impact of both bilinear and quadratic based energy-mapping methods on linear attenuation coefficients, attenuation maps and corrected PET images was assessed at different CT tube voltages. Attenuation maps were calculated from CT images of a cylindrical polyethylene phantom containing different concentrations of K<sub>2</sub>HPO<sub>4</sub> in water. Correlation coefficients and best regression fit equations were calculated for both methods. Phantom and rodent PET/CT images were used to assess improvements in image quality and quantitative accuracy. It was observed that the slopes of the bilinear calibration curves for CT numbers greater than 0 HU increase with increasing tube voltage. In addition, higher correlation coefficients were obtained for the quadratic compared [...]

### Reference

PRASAD, Rameshwar, *et al.* CT-Based Attenuation Correction on the FLEX Triumph Preclinical PET/CT Scanner. *IEEE Transactions on Nuclear Science*, 2011, vol. 58, no. 1, p. 66-75

DOI : 10.1109/TNS.2010.2087416

Available at:

<http://archive-ouverte.unige.ch/unige:23506>

Disclaimer: layout of this document may differ from the published version.



UNIVERSITÉ  
DE GENÈVE

# CT-Based Attenuation Correction on the FLEX Triumph Preclinical PET/CT Scanner

Rameshwar Prasad, Mohammad R. Ay, *Member, IEEE*, Osman Ratib, and Habib Zaidi, *Senior Member, IEEE*

**Abstract**—Positron Emission Tomography (PET) has emerged as a valuable molecular imaging modality for quantitative measurement of biochemical processes *in vivo* in the clinical and preclinical imaging domains. However, PET imaging suffers from various physical degrading factors including photon attenuation, which can be corrected using CT-based attenuation correction (CTAC) on combined PET/CT scanners. The attenuation map is calculated by converting CT numbers derived from low-energy polyenergetic x-ray spectra to linear attenuation coefficients at 511 keV. Generation of accurate attenuation maps is crucial for reliable attenuation correction of PET data and hence is a prerequisite for accurate quantification of biological processes. In this study, we implemented the CTAC procedure on the FLEX Triumph™ preclinical PET/CT scanner and evaluated tube voltage dependence for different kVps (40, 50, 60, 70, and 80). The quantitative impact of both bilinear and quadratic based energy-mapping methods on linear attenuation coefficients, attenuation maps and corrected PET images was assessed at different CT tube voltages. Attenuation maps were calculated from CT images of a cylindrical polyethylene phantom containing different concentrations of  $K_2HP O_4$  in water. Correlation coefficients and best regression fit equations were calculated for both methods. Phantom and rodent PET/CT images were used to assess improvements in image quality and quantitative accuracy. It was observed that the slopes of the bilinear calibration curves for CT numbers greater than 0 HU increase with increasing tube voltage. In addition, higher correlation coefficients were obtained for the quadratic compared to the bilinear energy-mapping method. Tube voltage of 70 kVp produced the smallest relative error and higher correlation coefficient compared to other tube voltages. For low concentrations of  $K_2HP O_4$ , the mean relative difference (in %) between theoretical and calculated attenuation coefficients when using bilinear and quadratic energy-mapping methods are  $1.39 \pm 1.9$  and  $1.33 \pm 1.8$ , respectively. They are  $2.78 \pm 1.3$  and  $2.5 \pm 1.3$ , respectively, for high concentrations of  $K_2HP O_4$ . As expected, higher activity concentrations were obtained for PET after attenuation correction. The increased PET signal for mouse tissues ranged between 21 and 31% for bilinear energy-mapping and between 21.8 and 35% for quadratic energy-mapping, whereas these varied from 40 to 51% and from 41 to 56%, respec-

tively, for rat tissues. For biological tissues having a high atomic number such as bone, the quadratic energy-mapping method produced slightly improved results compared to the bilinear energy-mapping method. Phantom and rodent PET studies were successfully corrected for photon attenuation using the developed CTAC procedure.

**Index Terms**—Attenuation correction, energy-mapping, PET/CT, quantification, small-animals.

## I. INTRODUCTION

**P**OSITRON emission tomography (PET) has emerged as a revolutionary molecular imaging technology for qualitative assessment and quantitative measurement of biochemical processes *in vivo* in the clinical and preclinical imaging domains. However, the technique suffers from many physical degrading factors with photon attenuation being one of the major issues impacting image quality and quantitative analysis of PET images [1]. The magnitude of photon attenuation in small-animal PET is not as large as in clinical imaging situations. Indeed, 5 cm of soft tissue, the approximate transverse size of a 250 g rat, may absorb 40% of 511 keV photons [2]. This proves that attenuation correction (AC) is still potentially important for accurate estimation of tracer uptake in high-resolution preclinical PET imaging [3]. Through knowledge of the attenuation properties of the object being scanned, the measurement along each line of response can be corrected for photon attenuation. Various strategies were developed for the purpose of attenuation correction in PET [1]. CT-based attenuation correction (CTAC) is one of the well established techniques on combined PET/CT scanners owing to the low statistical noise and high-quality anatomical information, small crosstalk between PET annihilation photons and low energy x-rays, and higher throughput imaging protocols [4]. However, accurate and robust conversion of CT numbers derived from low-energy polyenergetic x-ray spectra of a CT scanner to linear attenuation coefficients at 511 keV has become essential for accurate correction of the corresponding PET data. Several strategies have been reported in the literature such as segmentation [4], scaling [5], hybrid (segmentation/scaling) [6], bilinear or piece-wise scaling [7] and dual-energy decomposition methods [8]. The bilinear conversion method uses a linear relationship between CT numbers and linear attenuation coefficients of materials at 511 keV with one slope for soft tissue regions (air-water segment) and another slope for bone regions (water-bone segment) [9].

CT numbers in the range  $-1000 < HU < 0$  are considered to represent regions with a mixture of air and soft tissue whereas positive CT numbers ( $HU > 0$ ) represent regions with

Manuscript received December 07, 2009; revised March 29, 2010; accepted September 20, 2010. Date of publication November 09, 2010; date of current version February 09, 2011. This work was supported by the Swiss National Science Foundation under Grant SNSF 31003A-125246.

R. Prasad and O. Ratib are with the Division of Nuclear Medicine, Geneva University Hospital, CH-1211 Geneva, Switzerland (e-mail: rameshwar.prasad@unige.ch; osman.ratib@hcuge.ch).

M. R. Ay is with the Department of Medical Physics and Biomedical Engineering, Tehran University of Medical Sciences, Research Center for Science and Technology in Medicine, Tehran, Iran and also with the Research Institute for Nuclear Medicine, Tehran University of Medical Sciences, Tehran, Iran (e-mail: mohammadreza\_ay@tums.ac.ir).

H. Zaidi is with the Division of Nuclear Medicine, Geneva University Hospital, CH-1211 Geneva, Switzerland and also with the Geneva Neuroscience Center, Geneva University, CH-1211 Geneva, Switzerland (e-mail: habib.zaidi@hcuge.ch).

Color versions of one or more of the figures in this paper are available online at <http://ieeexplore.ieee.org>.

Digital Object Identifier 10.1109/TNS.2010.2087416

a mixture of soft tissue and bone. Other variants to the linear relationship were also proposed through the use of nonlinear regression such as quadratic polynomial mapping algorithms [10]. Although the bilinear conversion method remains the most widely used technique, the quadratic polynomial energy-mapping method is an appealing approach [10]. Energy-mapping methods are generally derived at a preset tube voltage and current. These methods are widely used and validated on clinical PET systems [11]; however, they still need to be thoroughly investigated on dedicated high resolution, small field-of-view scanners such as those used for small-animal imaging.

The quantitative capabilities of the commercially available FLEX Triumph™ (Gamma Medica-Ideas, Norridge, CA) pre-clinical PET/CT platform installed in our department are being characterized [12]; however, the lack of reliable image correction methodologies necessitated the implementation of CTAC on this system as a first step to achieve our endeavors. In this work, we implemented and evaluated tube voltage-dependent attenuation correction on this preclinical PET/CT scanner. Improvements in image quality and quantitative capability of pre-clinical PET images corrected for attenuation using attenuation maps generated using both bilinear and quadratic polynomial energy-mapping methods were also assessed.

## II. MATERIALS AND METHODS

### A. System Description

PET and CT data were acquired using the commercially available FLEX Triumph™ preclinical PET/CT scanner (Gamma Medica-Ideas, Norridge, CA). Both PET and CT subsystems are mounted on the same gantry allowing functional and anatomical imaging without moving the animal (other than table translation). The X-PET subsystem is based on detector blocks arranged in 48 rings having a 10 cm transaxial field-of-view (FOV) and 11.6 cm axial FOV. The PET detector array consists of 11,520 individual Bismuth Germanate (BGO) crystals arranged in 48 rings and 180 blocks. The dimension of each crystal is  $2.3 \times 2.3 \times 10 \text{ mm}^3$  in the axial, transaxial, and radial direction, respectively. This optimal design allows achieving unique properties such as low-cost, high-sensitivity and large axial FOV using an inexpensive crystal material arranged in pixilated ring geometry. The scanner incorporates the photomultiplier (PMT)-quadrant-sharing (PQS) method [13] which maximizes the number of crystals per PMT that can be decoded, thus improving the system's spatial resolution. The sensitivity and light output are maximized by using 96% crystal-packing fraction and no light-guides, respectively. High yield pileup event recovery (HYPER) electronic processing technology is used to improve count rate performance [14]. The detector blocks are circularized by slightly grinding each block on the PMT side into a pentagon shape and having the two end-rows of crystals in each block tapered [15]–[17]. The PET scanner has a spatial resolution of 1.8 mm full-width at half-maximum (FWHM) and sensitivity near 8% at the center of the FOV [12]. The high-resolution microCT subsystem is configured with a CMOS x-ray detector coupled to a scintillator [18] and a standard self-contained, air-cooled x-ray tube operating in the range of 40–80 kVp having a standard micro-focus

tube of a  $75 \mu\text{m}$  focal spot with 40 W total power. The CT tube has target material of tungsten with cone angle of 38 degree. The detector is made of CsI flipped scintillator material with pixel array of  $2240 \times 2368$  and a pixel size of  $50\text{-}\mu\text{m}$  [19].

### B. Data Acquisition and Processing

PET scans were acquired with a 250–750 keV energy window and 12 ns timing window. Coincident events acquired in list-mode format were first Fourier rebinned into 2D sinograms, and then reconstructed using 2D ordered subsets-expectation maximization (OS-EM) algorithm (4 iterations and 10 subsets), resulting in  $0.4 \times 0.4 \times 0.4 \text{ mm}^3$  voxel size for a  $256 \times 256 \times 256$  image volume.  $^{18}\text{F}$ -fluorodeoxyglucose (FDG) was used as tracer for PET studies. CT scans were acquired using tube voltages varying between 40 and 80 kVp and optimized tube current. The gantry rotated in continuous flying mode. A total of 512 projections were acquired in a full  $360^\circ$  scan with  $2240 \times 2368$  projection matrix size. Images were reconstructed using a modified 3D cone-beam Feldkamp algorithm resulting in  $0.17 \times 0.17 \times 0.17 \text{ mm}^3$  voxel size for a  $512 \times 512 \times 512$  image volume. CT images were downsampled to match the bin size of PET images. This was followed by energy conversion of CT images using experimentally derived bilinear and quadratic polynomial energy-mapping methods to match PET's energy. Gaussian smoothing was then applied using an appropriate Gaussian kernel (FWHM = 1.8 mm) to match PET's spatial resolution. The resulting attenuation maps were then forward projected using ray tracing based on Siddon's algorithm [20] implemented in C++ programming environment. The forward projected sinograms were then exponentiated to generate attenuation correction factors (ACFs). The measured PET sinogram was then multiplied by the generated ACFs to obtain the attenuation corrected PET sinograms. The multiplicative ACF for a given path length is calculated according to:

$$ACF = \exp\left(\int \mu_{511 \text{ keV}}(x) dx\right) \quad (1)$$

where  $\mu_{511 \text{ keV}}$  is the linear attenuation coefficient at 511 keV.

The attenuation corrected PET sinogram was then reconstructed using the same technique used for the uncorrected data to obtain the final CT-based attenuation corrected PET images. The strategy followed for implementation of the CT-based attenuation correction technique is described elsewhere[2].

### C. Conversion of CT Images to $\mu$ Maps

A specially designed polyethylene cylindrical phantom ( $\phi 70 \pm 0.5 \text{ mm}$ ), containing 16 cylindrical holes ( $\phi 5 \pm 0.1 \text{ mm}$ ), was scanned on the CT subsystem of the combined PET/CT scanner by varying CT tube voltages between 40 to 80 kVp. To simulate different types of biological materials, thirteen plugs were filled with a mixed solution of  $\text{K}_2\text{HPO}_4$  and water, with concentrations varying between 80 and 1040 mg/cc (ranging between 0.1 and  $0.155 \text{ cm}^{-1}$  at 511 keV) along with three additional plugs containing water, air and lung equivalent tissue (Fig. 1(a)). The CT image values were extracted from volumes

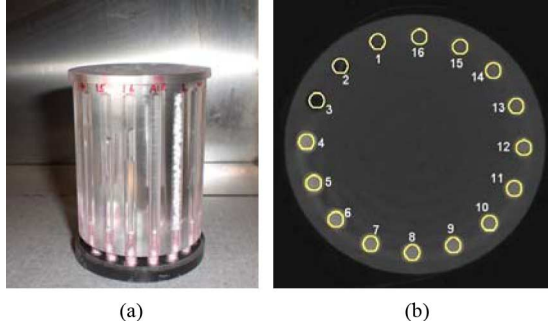


Fig. 1. (a) Photograph of the specially designed polyethylene cylindrical phantom containing 16 cylindrical holes (b) Transverse CT image of the calibration phantom showing the location of defined VOIs.

of interest (VOIs) of dimensions  $0.4 \times 0.4 \times 0.17 \text{ mm}^3$  in each image corresponding to the location of the samples (Fig. 1(b)).

The theoretical linear attenuation coefficients ( $\mu$ ) for each material were calculated using the NIST XCOM photon cross section library [21], and served as reference for evaluation of phantom studies. The known  $\mu$  of each material was subsequently plotted against its CT number. In the CT energy range, Compton scattering dominates the  $\mu$  coefficient of low-Z materials (such as water and soft tissue), while photoelectric effect dominates the  $\mu$  coefficient of high-Z materials (such as bone). Thus, different scaling factors are used to transform CT numbers into a  $\mu$ -map at 511 keV for different tissues. For  $\text{HU} \leq 0$  the plotted curve was fitted only linearly. However, for  $\text{HU} > 0$  both a linear and quadratic polynomial functions were fitted to the data points with 95% confidence interval. The two fitted functions provided bilinear and quadratic polynomial energy-mapping curves for use in attenuation correction of PET studies.

The bilinear energy-mapping method uses the following equations [11]:

$$\begin{aligned} \mu [\text{cm}^{-1}] &= 9.6 \times 10^{-5} \times (\text{HU} + 1000) \quad \forall \text{HU} \leq 0 \\ \mu [\text{cm}^{-1}] &= a \times (\text{HU} + 1000) + b \quad \forall \text{HU} > 0. \end{aligned} \quad (2)$$

The quadratic energy mapping method is defined by the following equations [10]:

$$\begin{aligned} \mu [\text{cm}^{-1}] &= 9.6 \times 10^{-5} \times (\text{HU} + 1000) \quad \forall \text{HU} \leq 0 \\ \mu [\text{cm}^{-1}] &= a \times (\text{HU} + 1000)^2 \\ &\quad + b \times (\text{HU} + 1000) + c \quad \forall \text{HU} > 0. \end{aligned} \quad (3)$$

#### D. Phantom and Rodent Studies

Three phantom studies (of different size) were performed for validation purposes. A uniform cylindrical phantom of 2.5 cm diameter and 14 cm length was filled with uniformly distributed mixture of water and 3 MBq of  $^{18}\text{F}$ . The second phantom used is the NEMA NU 4-2008 image quality phantom [22] filled with a mixture of water and 4 MBq of  $^{18}\text{F}$ . The third one is the Micro-deluxe Phantom<sup>TM</sup> (Model ECT/DLX/MMP) filled with a mixture of water and 8 MBq of  $^{18}\text{F}$ . The phantom consists of a 5-cm outer diameter and 4.5-cm inner diameter cylinder that

can accommodate hot or cold rod inserts. The rods are grouped into sectors with diameters of 4.8 mm, 4.0 mm, 3.2 mm, 2.4 mm, 1.6 mm, and 1.2 mm.

PET imaging was performed for the above mentioned phantoms for a duration of 10 minutes (except the uniform cylindrical phantom which was scanned for 5 minutes) and followed immediately by a CT scan. Rodent studies included one healthy mouse (24 g) and one rat (260 g). The mouse and rat were anesthetized with 2% of isoflurane and injected intravenously in the tail with about 10 and 38 MBq of  $^{18}\text{F}$ -FDG, respectively. PET acquisitions were performed for 10 minutes covering the whole-body for the mouse study whereas only the head region of the rat was covered. A CT scan of 2 minutes was then performed for each animal after PET acquisition of the same region. All PET studies were performed in an activity/count rate regime resulting in a low random coincidence rate. Activity was measured with a regularly calibrated dose calibrator (MED Dose Calibrator Isomed 2000). The calibration of emission activity values to actual activity concentration was performed using a small cylinder (2.5 cm diameter) filled with a mixture of 3 MBq of  $^{18}\text{F}$  and water. The cylinder was scanned for 2 hours using an energy window of 250–750 keV and 12 ns timing window. The PET emission data were corrected for attenuation. The actual activity concentration in the cylinder was computed from the activity, measured in a dose calibrator, and the volume of the sample. The computed activity concentration was related to a region of interest in the PET image. The resulting calibration factor (CF) that relates activity concentration to reconstructed counts per voxel was calculated using the following equation:

$$CF = \frac{A_{\text{measured}}}{A_{\text{cal}}} \quad (4)$$

where  $A_{\text{cal}}$  is computed as follows:

$$A_{\text{cal}} = \left( \frac{A}{V} \right) \times N \times \exp \left( -0.693 \times \frac{t}{T_{1/2}} \right)$$

where  $A$  is the activity in the phantom measured in a dose calibrator,  $V$  is the volume of the phantom,  $N$  is the branching ratio of positron decay of the radionuclide, and  $t$  is the time delay from initial measurement to the start of the scan, and  $T_{1/2}$  is the half-life of the radionuclide used.

#### E. Analysis

A VOI- and line profile-based quantitative analysis was performed on phantom and rodent studies for assessment of the quality of  $\mu$ -maps and CTAC procedure using both energy-mapping methods. VOIs of dimension  $0.4 \times 0.4 \times 0.17 \text{ mm}^3$  were defined on regions of the  $\mu$ -map corresponding to different concentrations of  $\text{K}_2\text{HPO}_4$  solution and the mean  $\mu$  value was calculated. The obtained results were then compared with the theoretical  $\mu$  estimated using the XCOM data tables [21]. The analysis was performed on 2 datasets corresponding to regions with low concentration ( $\leq 160 \text{ mg/cc}$ ) of  $\text{K}_2\text{HPO}_4$ , representing soft tissue, and regions with high concentration ( $> 160 \text{ mg/cc}$ ) of  $\text{K}_2\text{HPO}_4$ , representing high density tissues for both energy-

mapping methods. Four and 11 data points were considered for representation of low and high concentration, respectively.

Four VOIs of dimension  $6.5 \times 6.5 \times 0.4 \text{ mm}^3$  were drawn on the central slice of the uniform cylindrical phantom and uniform compartment of the NEMA image quality phantom for both uncorrected and attenuation corrected PET data sets. Likewise, three VOIs of the same size were drawn on the largest diameter rod of the Micro-deluxe phantom. VOI drawing and image analysis were performed using AMIDE [23] and PMOD software (PMOD Technologies Ltd, Zurich, Switzerland). The mean, standard deviation and coefficients of variation (CV) were also computed for each VOI.

The CV, which is a measure of the magnitude of noise in the reconstructed image, was calculated for the phantom studies by computing  $\sigma/\mu_{\text{mean}}$ , where  $\sigma$  and  $\mu_{\text{mean}}$  are the standard deviation and mean of the pixel values within the above mentioned VOIs, respectively. In addition, line profiles were drawn on uncorrected and attenuation corrected PET images and compared to actual activity line profiles. Percent differences from actual values were also calculated. For the mouse study, several VOIs of dimension  $4.0 \times 4.0 \times 0.4 \text{ mm}^3$  were drawn on brain, heart, and bladder regions whereas smaller VOIs ( $2.8 \times 2.8 \times 0.4 \text{ mm}^3$ ) was drawn for bone (vertebra) region. Likewise, VOIs of dimension  $8.0 \times 8.0 \times 0.4 \text{ mm}^3$  were drawn on the brain and striatum whereas smaller VOIs ( $2.8 \times 2.8 \times 0.4 \text{ mm}^3$ ) were drawn on the bony region of the rat. The increased percentages of PET intensities after attenuation correction as compared to uncorrected images were calculated for mouse and rat tissues using both energy-mapping methods. Statistical analysis using Student's t-test was performed to assess significant differences between attenuation corrected PET images using both energy-mapping methods.

### III. RESULTS

#### A. Conversion of CT Images to $\mu$ -Maps

Linear attenuation coefficients for the different materials present in the calibration phantom were plotted as a function of CT numbers. Curve fitting using both linear and quadratic polynomial functions was performed to determine the fitting parameters as shown in Fig. 2. As mentioned earlier, CT data were obtained at several x-ray tube voltages ranging from 40 to 80 kVp. The fitting parameters and correlation coefficients ( $R^2$ ) for both bilinear and quadratic energy-mapping methods at different CT tube voltages are shown in Table I.

The obtained  $\mu$ -maps were compared with the theoretical estimates calculated using the XCOM photon cross section library [21] for different tube voltages. Table II summarizes the mean relative difference between measured and theoretical attenuation coefficients for the bilinear method when using different tube voltages. The results show that a tube voltage of 70 kVp produced the smallest relative error and higher correlation coefficient compared to other tube voltages given the calibration curve was obtained at this tube voltage. This tube voltage was selected for further assessment.

Table III summarizes the mean relative difference between measured and theoretical attenuation coefficients for the various

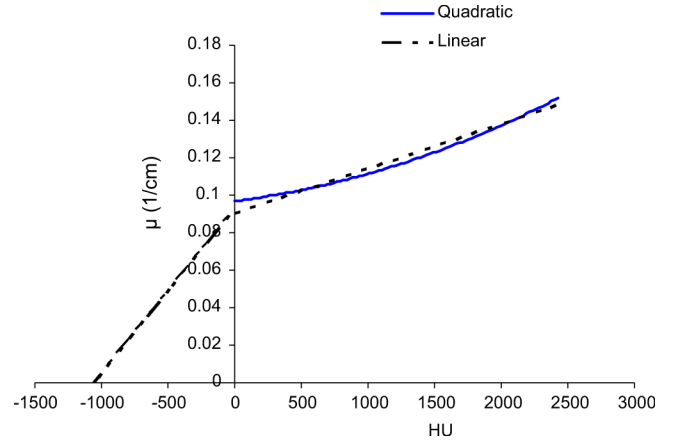


Fig. 2. Representative plots of bilinear and quadratic fitting of the calibration curves at 70 kVp and 275  $\mu\text{A}$ .

TABLE I  
SUMMARY OF FITTING PARAMETERS AND CORRELATION COEFFICIENTS ( $R^2$ )  
FOR BOTH BILINEAR AND QUADRATIC ENERGY-MAPPING METHODS

kVp	Bilinear energy-mapping method			$R^2$
	$a(\text{cm}^{-1}) \times 10^{-5}$	$b(\text{cm}^{-1}) \times 10^{-2}$		
40	1	8.60		0.90
50	2	8.60		0.90
60	2	8.62		0.89
70	9	9.20		0.98
80	9	8.80		0.93
kVp	Quadratic energy-mapping method			$R^2$
	$a(\text{cm}^{-1}) \times 10^{-9}$	$b(\text{cm}^{-1}) \times 10^{-6}$	$c(\text{cm}^{-1}) \times 10^{-2}$	
40	3	0.70	9.50	0.96
50	4	0.30	9.60	0.96
60	5	3.00	9.70	0.97
70	6	9.00	9.50	0.97
80	6	6.00	9.30	0.93

samples when using two different energy-mapping methods. The results presented were averaged for low and high concentrations of  $\text{K}_2\text{HPO}_4$  to allow modelling of soft tissue and bony structures (Fig. 3). The error bars in Fig. 3 represent the standard deviation of data points for various ROIs defined on low and high and low concentration regions. For low concentrations of  $\text{K}_2\text{HPO}_4$ , the mean relative difference (in %) between theoretical and calculated attenuation coefficients when using bilinear and quadratic energy-mapping methods are  $1.39 \pm 1.9$  and  $1.33 \pm 1.8$ , respectively. They are  $2.78 \pm 1.3$  and  $2.50 \pm 1.3$  for high concentrations of  $\text{K}_2\text{HPO}_4$ , respectively. Hence, both energy-mapping methods produce quite similar relative difference for low concentrations of  $\text{K}_2\text{HPO}_4$ . However, for higher concentrations of  $\text{K}_2\text{HPO}_4$ , the quadratic energy-mapping method

TABLE II  
MEAN RELATIVE DIFFERENCE (IN %) BETWEEN ATTENUATION COEFFICIENTS DERIVED USING THE BILINEAR METHOD FOR DIFFERENT COMBINATIONS OF kVPS AND THE THEORETICAL LINEAR ATTENUATION COEFFICIENTS CALCULATED USING THE XCOM PHOTON CROSS-SECTION LIBRARY FOR VARIOUS REGIONS CORRESPONDING TO DIFFERENT CONCENTRATIONS OF  $K_2HPO_4$

Material	CT values (70 kVp)	$\mu$ at 511keV [ $cm^{-1}$ ]	40 kVp	50 kVp	60 kVp	70 kVp	80 kVp
Air	-1000	0.000	0.00	0.00	0.00	0.00	0.00
H <sub>2</sub> O	0.0	0.096	0.69	0.77	0.92	0.23	0.11
0.08*	440.0	0.100	2.11	2.15	2.51	0.34	2.13
0.16	591.0	0.105	4.53	2.17	2.52	3.60	2.14
0.24	810.5	0.109	3.23	4.85	3.62	3.01	4.32
0.32	1014.3	0.114	3.27	4.15	3.71	4.10	4.13
0.4	1283.7	0.118	4.37	5.60	4.42	3.20	4.32
0.48	1450.5	0.123	4.38	3.60	3.15	1.26	3.78
0.56	1760.7	0.128	2.73	2.90	1.89	2.10	2.43
0.64	1954.8	0.132	2.46	2.66	1.12	1.80	2.45
0.72	2083.1	0.137	3.15	1.36	1.88	1.23	0.86
0.8	2104.0	0.141	2.30	1.52	1.56	1.38	0.61
0.88	2247.2	0.146	1.83	1.98	1.72	3.21	2.11
0.96	2380.3	0.151	5.13	5.96	3.12	4.20	6.43
1.04	2427.6	0.155	5.60	5.40	5.80	5.06	4.80
mean $\pm$ SD	-	0.12 $\pm$ 0.03	3.05 $\pm$ 1.57	3.00 $\pm$ 1.84	2.52 $\pm$ 1.48	2.31 $\pm$ 1.58	2.70 $\pm$ 1.88

\*Concentration (in g/cc) of  $K_2HPO_4$  in water

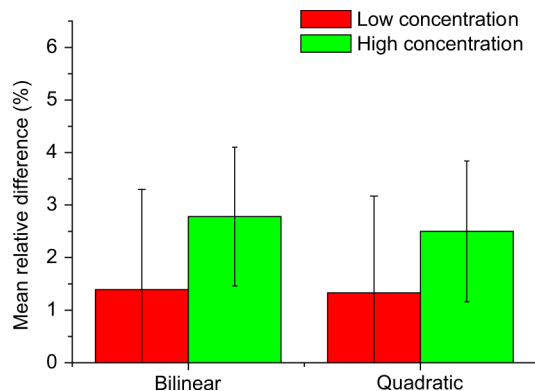


Fig. 3. Mean relative difference of linear attenuation coefficients ( $\mu$ ) calculated using the two energy-mapping methods for low ( $\leq 160$  mg/cc) and high ( $> 160$  mg/cc) concentrations of  $K_2HPO_4$  solution modeling soft tissue and bony structures, respectively.

results in relatively lower relative difference compared to the bilinear method. The original transverse CT image of the NEMA image quality phantom together with a horizontal line profile showing actual and resulting CT numbers is shown in Fig. 4. The beam hardening effect is clearly visible.

The  $\mu$ -maps along with line profiles of the NEMA image quality phantom generated using both energy-mapping methods are shown in Fig. 5. Similar results are shown for the mouse in Fig. 6.

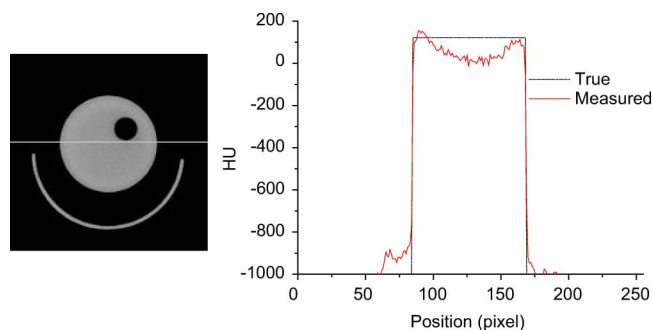


Fig. 4. Transaxial CT images of the NEMA image quality phantom (left) and its corresponding horizontal line profile (right).

### B. Phantom and Rodent Studies

PET images of a transverse slice of the cylindrical, NEMA NU 4- 2008 image quality, and Micro-deluxe phantoms are shown before and after attenuation correction using both energy-mapping methods in Figs. 7–9, respectively. Horizontal line profiles of the images of various phantoms along with the actual activity concentration are also shown. The percentage coefficients of variation (CV) in the drawn VOIs for various phantoms of are shown in Table IV. The mean % CV derived from uncorrected emission data was significantly different from all corrected data ( $P < 0.005$ ).

TABLE III  
MEAN RELATIVE DIFFERENCE (IN %) BETWEEN THE ATTENUATION COEFFICIENTS OBTAINED WHEN USING TWO ENERGY-MAPPING METHODS AND THE THEORETICAL LINEAR ATTENUATION COEFFICIENTS COMPUTED USING THE XCOM PHOTON CROSS-SECTION LIBRARY FOR DIFFERENT REGIONS WITHIN THE PHANTOM

Material	$\mu$ at 511 keV [ $\text{cm}^{-1}$ ]	Bilinear	Quadratic
Air	0.000	0.00	0.00
H <sub>2</sub> O	0.096	0.23	0.23
0.08*	0.100	0.34	0.31
0.16	0.105	3.60	3.46
0.24	0.109	3.01	3.00
0.32	0.114	4.10	4.10
0.4	0.118	3.20	3.19
0.48	0.123	1.26	1.00
0.56	0.128	2.10	1.19
0.64	0.132	1.80	1.60
0.72	0.137	1.23	1.18
0.8	0.141	1.38	1.01
0.88	0.146	3.21	2.90
0.96	0.151	4.20	3.88
1.04	0.155	5.60	4.99
mean $\pm$ SD	0.117 $\pm$ 0.03	2.35 $\pm$ 1.65	2.10 $\pm$ 1.53

\*Concentration (in g/cc) of K<sub>2</sub>HPO<sub>4</sub> in water

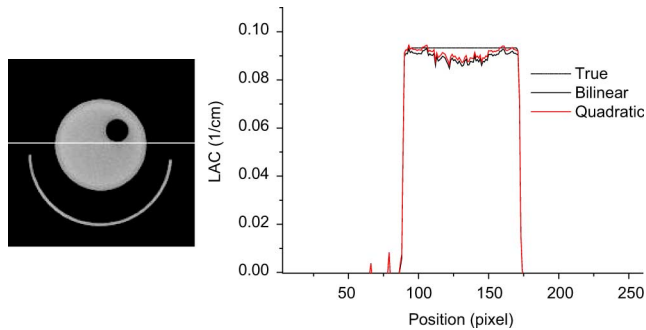


Fig. 5. Attenuation map of the NEMA phantom (left) and corresponding horizontal line profile of the actual and  $\mu$ -maps generated using both bilinear and quadratic polynomial methods (right).

Figs. 10 and 11 show the correlated CT image, uncorrected and attenuation corrected PET images of the mouse and rat using both energy-mapping methods. Horizontal line profiles passing through the heart and brain, respectively, are also shown. Fig. 12 illustrates the percent increment of PET activity concentration when using CTAC in rodent PET imaging for both energy-mapping methods. The increased image intensities for different mouse tissues are in the range 21–31% for bilinear and 21.8–35% for quadratic energy-mapping. They are in the range 40–51% and 41–56%, respectively, for the rat.

The error bars reflect statistical analysis for several VOIs drawn on various parts of rodents’ body including the brain, heart, bone and bladder. Statistical analysis using student’s t-test at 0.05 significance level did not reveal statistically significant differences between attenuation corrected PET images using both energy-mapping methods for experimental phantoms and preclinical studies. However, for high atomic

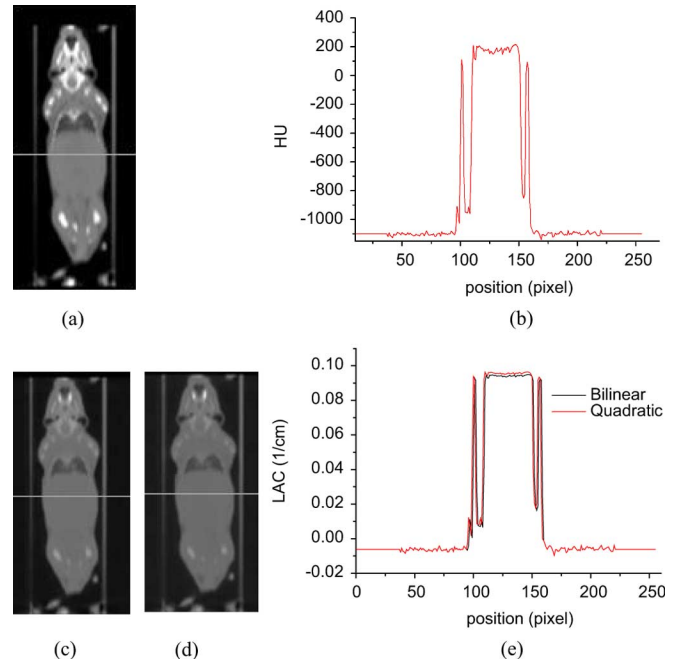


Fig. 6. Coronal CT images of a mouse showing (a) The original CT image and (b) its corresponding horizontal line profile (c) The generated attenuation maps using the bilinear and (d) Quadratic polynomial methods (e) The corresponding horizontal line profiles are also shown.

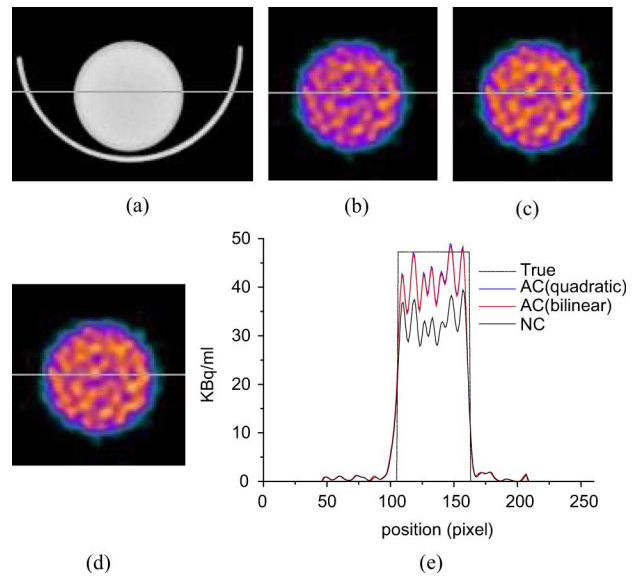


Fig. 7. Transaxial images of the uniform cylindrical phantom showing (a) CT image (b) Uncorrected PET image (c) CT-based attenuation corrected PET image using the bilinear energy-mapping method (d) Attenuation corrected PET image using the quadratic energy-mapping method, and (e) Corresponding horizontal profiles through images shown in (b)–(d).

number tissues such as bone, the quadratic energy-mapping method produced slightly enhanced increment of PET activity concentration than the bilinear energy-mapping method for attenuation corrected as compared to uncorrected PET images.

#### IV. DISCUSSION

Accurate quantification in PET requires precise correction for the many physical degrading factors out of which photon at-

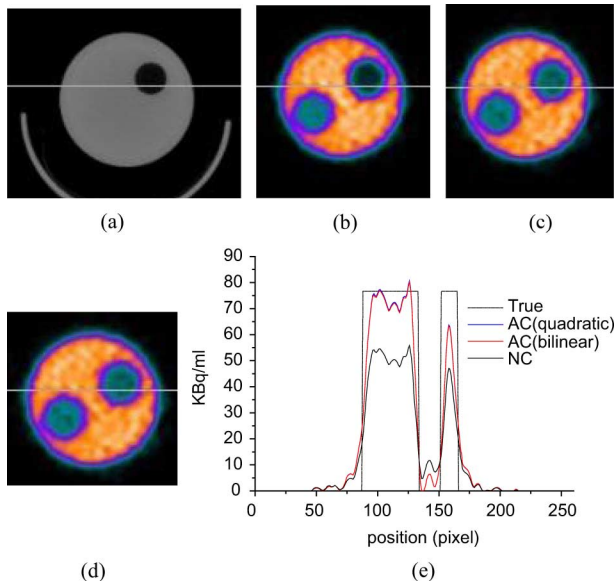


Fig. 8. Transaxial images of the NEMA image quality phantom showing (a) CT image (b) Uncorrected PET image (c) Attenuation corrected PET image using the bilinear energy-mapping method (d) Attenuation corrected PET image using the quadratic energy-mapping method, and (e) The corresponding horizontal profiles through images shown in (b)–(d).

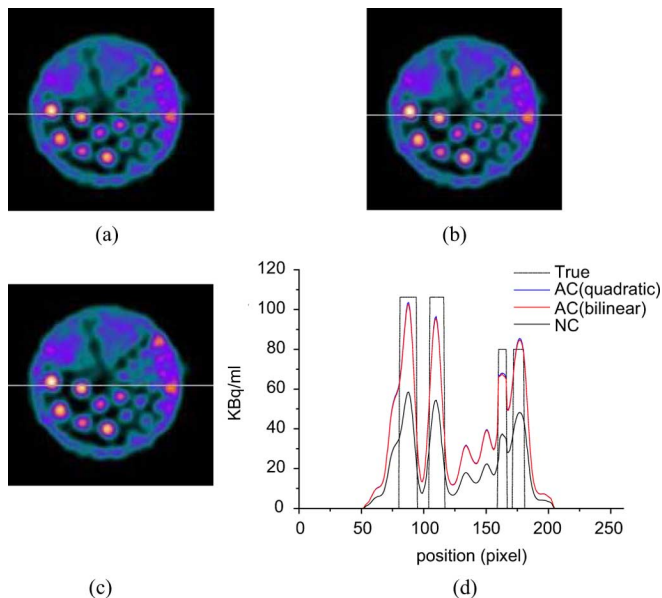


Fig. 9. Transaxial images of the Micro-deluxe phantom showing (a) Uncorrected PET image (b) Attenuation corrected PET image using the bilinear energy-mapping method (c) Attenuation corrected PET image using the quadratic energy-mapping method (d) The corresponding horizontal profiles through images shown in (a)–(c).

Attenuation is the major one. Attenuation correction of PET data requires an accurate attenuation map which represents the spatial distribution of linear attenuation coefficients at 511 keV for the volumes under study. Two main classes of method have emerged for generation of attenuation maps: transmissionless and transmission-based methods. Transmissionless correction methods rely on simple calculated techniques such as those used for brain imaging or more sophisticated algorithms allowing simultaneous modeling of attenuation and emission distributions

TABLE IV  
COMPARISON OF CV (%) BETWEEN UNCORRECTED AND ATTENUATION CORRECTED PET IMAGES (USING BILINEAR AND QUADRATIC ENERGY-MAPPING METHODS)

Study	CV		
	Uncorrected	AC using bilinear method	AC using quadratic method
Uniform Phantom	10.57	10.09	10.11
NEMA Phantom	5.21	5.17	5.17
Micro-deluxe Phantom	6.23	6.00	5.80
Mouse	15.11	14.23	14.35
Rat	23.60	22.41	22.42

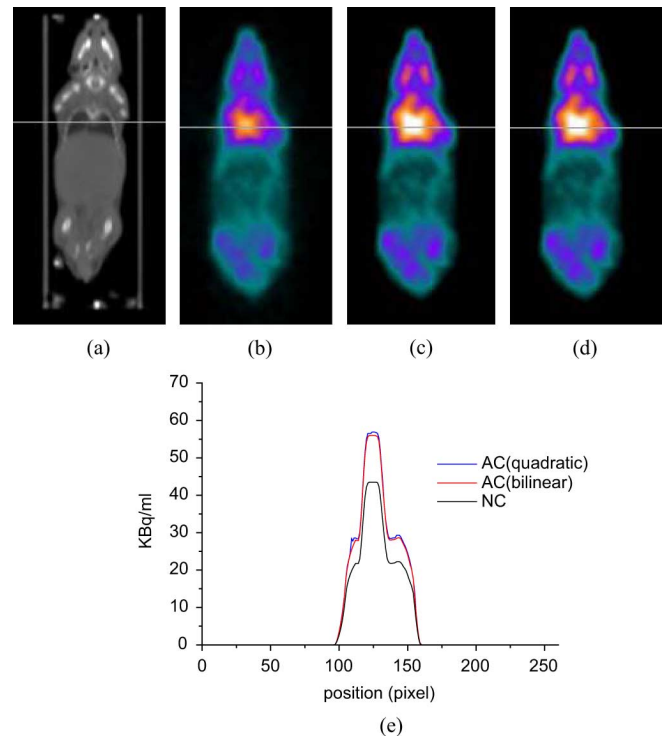


Fig. 10. Coronal images of the mouse showing (a) CT image (b) Uncorrected PET image (c) Attenuation corrected PET image using the bilinear energy-mapping method (d) Attenuation corrected PET image using the quadratic energy-mapping method, and (e) Corresponding horizontal profiles through images shown in (b)–(d).

from a set of emission projections alone. Transmission-based methods include transmission imaging using external radionuclide sources, x-ray CT imaging and segmented MRI data. The advantage of using x-ray CT are the lower statistical noise, and unbiased and faster post-injection transmission scans, in addition to high resolution anatomical imaging offering improved localization capabilities that can not be obtained using radionuclide transmission scanning [24]. The use of CT images for attenuation correction requires transforming the polyenergetic CT data to linear attenuation coefficients at 511 keV. This can be

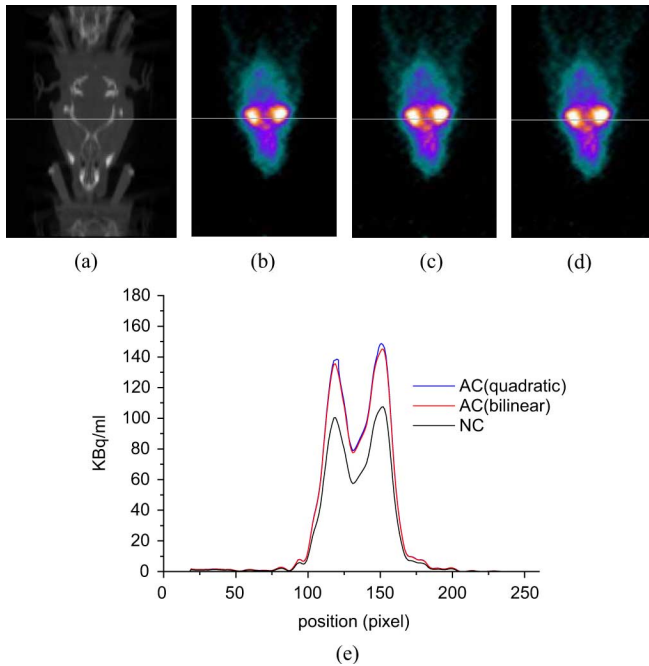


Fig. 11. Coronal images of the rat brain showing (a) CT image (b) Uncorrected PET image (c) Attenuation corrected PET image using the bilinear energy-mapping method (d) Attenuation corrected PET image using the quadratic energy-mapping method (e) Corresponding horizontal profiles through images shown in (b)–(d).

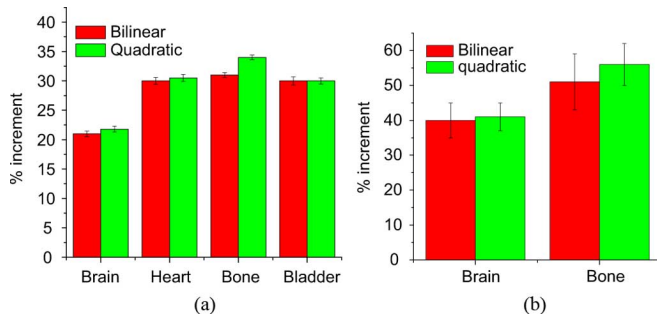


Fig. 12. Percent increment of PET activity concentration for (a) Mouse and (b) Rat when applying CTAC to PET data using both energy-mapping methods as compared to uncorrected PET images.

achieved by many conversion methods such as scaling, segmentation, and dual-energy decomposition methods [10]. In scaling methods, the attenuation map at 511 keV is estimated by multiplying the CT image of the subject by the ratio of attenuation coefficients of water at the photon energies of CT and PET. Segmentation methods segment the CT image into different regions representing different tissue properties, which are then assigned appropriate attenuation coefficients at 511 keV.

The software provided by the manufacturer of the FLEX Triumph™ preclinical PET/CT scanner installed in our facility does not incorporate CTAC utilities which are nowadays implemented by default on clinical scanners. This motivated its development and implementation on site. The general applicability of CTAC has already been proven in small-animal PET imaging [2], [3]. However, some pragmatic technical approaches still need to be explored. The strategy followed in the implementation of CTAC on this scanner follows the

general principles of the method described in [2]. However, some additional issues not sufficiently addressed in the early publications were investigated in this work. In particular, the effect of varying CT tube voltages was investigated through quantitative analysis of the created  $\mu$ -maps, generated ACFs and reconstructed PET images using experimental phantom and preclinical studies. Moreover, the practical application and impact of various calibration curve-based energy-mapping approaches for converting CT numbers to linear attenuation coefficients is studied for the bilinear and quadratic methods for water-bone segment.

A representative plot of the bilinear and quadratic polynomial fitting of the calibration curves at 70 kVp and 275  $\mu$ A is shown in Fig. 2. A plot discontinuity is observed at CT number corresponding to zero for quadratic polynomial fitting, which does not exist for the bilinear fitting. The reason for this is that we fitted the water-bone segment using both bilinear and quadratic polynomial whereas the air-water segment was fitted using linear curve fitting. The discontinuity can be removed by fitting the air-water segment with quadratic polynomial and this might improve the CT-based attenuation correction procedure. Nevertheless, both methods are reasonably successful in transforming rodent tissue CT values into 511 keV linear attenuation coefficients as demonstrated by our results. These results confirm and extend those shown previously by Chow *et al.* [2].

It was observed that increasing the tube voltage increases the slope of calibration curves for HU greater than zero (Table I). This can be explained as follows: the photoelectric interaction probability increases with decreasing tube voltage, particularly in materials with high atomic number. Moreover, since the derivation of calibration curves is based on CT numbers of air, water and bone, the tube voltage dependence of bone's CT number can be the ground for the difference in the slopes of calibration curves obtained at different CT tube voltages. Higher correlation coefficient and smallest relative error were obtained for CT tube voltage of 70 kVp for both energy-mapping methods. This setting could be considered as optimal tube voltage for PET/CT imaging studies (Table II). However, increasing the CT tube voltage increases the delivered radiation dose to the animal which is an important issue to consider. It was observed using experimental phantom studies that for all concentrations of  $K_2HPO_4$ , the relative difference between theoretical attenuation coefficients and those derived through energy-mapping are less than 5% (Table III). Moreover, for low concentrations of  $K_2HPO_4$ , the relative difference between theoretical attenuation coefficients and those derived by the two energy-mapping methods are almost identical. However, for higher concentrations of  $K_2HPO_4$ , the quadratic energy-mapping method has a smaller relative difference compared to the bilinear energy-mapping method (Fig. 4). The results of  $\mu$ -maps and PET data analysis are consistent with these observations. Therefore, in soft tissue regions where high atomic number tissues such as bones are absent, both energy-mapping methods produce similar results and may be used interchangeably for attenuation correction of PET data.

The % CV of PET activity concentration, which is considered as a measure of the SNR, is shown for various PET studies (Table IV). The mean % CV derived from uncorrected emission

data was significantly different from CT-based attenuation corrected data ( $p < 0.005$ ). There was no significant improvement of SNR in the attenuation corrected PET data since attenuation correction is a multiplicative process and as such will not improve the noise properties. It will at best result in similar noise properties but could be substantially improved if incorporated in an iterative reconstruction procedure using the well established attenuation weighted iterative reconstruction. Statistical analysis did not reveal statistically significant differences between PET images corrected using bilinear and quadratic energy-mapping methods for soft tissues. However, for high atomic number tissues such as bone, the quadratic energy-mapping method produced slightly improved results than bilinear energy-mapping methods.

The polyenergetic x-ray spectra used in CT imaging induces beam hardening artefacts caused by the absorption of low energy x-rays as they pass through the objects' volume. The direct outcome is that the linear attenuation coefficients calculated for thick object regions are lower than thin regions. This effect generates cupping and streak artefacts in the reconstructed CT images which propagate to PET images following application of the CTAC procedure [25]. Future work will focus on quantifying and correcting beam hardening effects. As mentioned earlier, as of present, the scanner manufacturer did not provide CTAC utilities on the FLEX Triumph™ preclinical PET/CT scanner. It would be interesting indeed to compare our results with those generated by the manufacturer's implementation should this option become available in the future. It should be noted that we considered only water-bone segment of calibration curves for deriving quadratic energy-mapping parameters. The air-water segment of calibration curves was fitted linearly. It would be interesting to consider fitting the air-water segment using quadratic energy-mapping calibration curve.

Despite the established fact that CTAC leads to more accurate quantification in high resolution preclinical PET imaging, further work is still needed to explore its broad potential, in particular in combination with Compton scatter and beam hardening correction of cone-beam CT data [26].

## V. CONCLUSION

Attenuation correction is of prime importance in preclinical PET imaging. The dependence of  $\mu$ -maps generated using two energy-mapping methods was evaluated for various x-ray CT tube voltages. In addition, the impact on resulting preclinical PET/CT studies was assessed. It was demonstrated that the slope of the energy-mapping curves for CT numbers greater than 0 HU increases with increasing tube voltages. In addition, higher correlation coefficients were obtained for the quadratic energy-mapping method compared to the bilinear energy-mapping method. In general, no statistically significant differences were observed on PET studies when using bilinear vs. quadratic energy-mapping methods for soft tissues. However, for high atomic number tissues such as bone, the quadratic energy-mapping method produced slightly improved results compared to the bilinear energy-mapping method, and as such this method is being used for attenuation correction of preclinical studies on the FLEX Triumph™ PET/CT scanner. Experimental phantom

and preclinical PET studies were successfully corrected for photon attenuation using the implemented CTAC procedure.

## ACKNOWLEDGMENT

The authors would like to thank Dr. P. Millet for providing some of the preclinical studies used in this work.

## REFERENCES

- [1] H. Zaidi, M.-L. Montandon, and A. Alavi, "Advances in attenuation correction techniques in PET," *PET Clinics*, vol. 2, pp. 191–217, 2007.
- [2] P. L. Chow, F. R. Rannou, and A. F. Chatziioannou, "Attenuation correction for small animal PET tomographs," *Phys. Med. Biol.*, vol. 50, pp. 1837–1850, 2005.
- [3] R. Yao, J. Seidel, J.-S. Liow, and M. V. Green, "Attenuation correction for the NIH ATLAS small animal PET scanner," *IEEE Trans. Nucl. Sci.*, vol. 52, pp. 664–668, 2005.
- [4] P. E. Kinahan, B. H. Hasegawa, and T. Beyer, "X-ray-based attenuation correction for positron emission tomography/computed tomography scanners," *Semin. Nucl. Med.*, vol. 33, pp. 166–179, Jul. 2003.
- [5] T. Beyer, P. E. Kinahan, D. W. Townsend, and D. Sashin, "The use of X-ray CT for attenuation correction of PET data," in *Proc. IEEE Nuclear Science Symp. and Medical Imaging Conf.*, Norfolk, VA, Nov. 1994, pp. 1573–1577.
- [6] P. E. Kinahan, D. W. Townsend, T. Beyer, and D. Sashin, "Attenuation correction for a combined 3D PET/CT scanner," *Med. Phys.*, vol. 25, pp. 2046–2053, Oct. 1998.
- [7] C. Bai, L. Shao, A. J. Da Silva, and Z. Zhao, "A generalized model for the conversion from CT numbers to linear attenuation coefficients," *IEEE Trans. Nucl. Sci.*, vol. 50, pp. 1510–1515, 2003.
- [8] M. J. Guy, I. A. Castellano-Smith, M. A. Flower, G. D. Flux, R. J. Ott, and D. Visvikis, "Detect-dual energy transmission estimation CT-for improved attenuation correction in SPECT and PET," *IEEE Trans. Nucl. Sci.*, vol. 45, pp. 1261–1267, 1998.
- [9] C. Burger, G. Goerres, S. Schoenes, A. Buck, A. H. Lonn, and G. K. Von Schulthess, "PET attenuation coefficients from CT images: Experimental evaluation of the transformation of CT into PET 511-keV attenuation coefficients," *Eur. J. Nucl. Med. Mol. Imag.*, vol. 29, pp. 922–927, 2002.
- [10] M. R. Ay, M. Shirmohammad, S. Sarkar, A. Rahmim, and H. Zaidi, "Comparative assessment of energy-mapping approaches in CT-based attenuation correction for PET," *Mol. Imag. Biol.*, Apr. 2010.
- [11] J. P. Carney, D. W. Townsend, V. Rappoport, and B. Bendriem, "Method for transforming CT images for attenuation correction in PET/CT imaging," *Med. Phys.*, vol. 33, pp. 976–983, Apr. 2006.
- [12] R. Prasad, O. Ratib, and H. Zaidi, "Performance evaluation of the FLEX Triumph™ X-PET scanner using the NEMA NU-04 standards," *J. Nucl. Med.*, vol. 51, pp. 1608–1615, 2010.
- [13] R. A. Ramirez, S. Liu, J. Liu, Y. Zhang, S. Kim, H. Baghaei, H. Li, Y. Wang, and W.-H. Wong, "High-resolution L(Y)SO detectors using PMT-quadrant-sharing for human and animal PET cameras," *IEEE Trans. Nucl. Sci.*, vol. 55, pp. 862–869, 2008.
- [14] W.-H. Wong, H. Li, J. Uribe, H. Baghaei, Y. Wang, and S. Yokoyama, "Feasibility of a high-speed gamma-camera design using the high-yield-pileup-event-recovery method," *J. Nucl. Med.*, vol. 42, pp. 624–632, 2001.
- [15] S. Xie, R. Ramirez, Y. Liu, T. Xing, J. Uribe, H. Li, Y. Wang, H. Baghaei, S. Kim, and W.-H. Wong, "A pentagon photomultiplier-quadrant-sharing BGO detector for a rodent research PET (RRPET)," *IEEE Trans. Nucl. Sci.*, vol. 52, pp. 210–216, 2005.
- [16] W.-H. Wong, H. Li, S. Xie, R. A.-R. Ramirez, R. S. K. A.-S. Kim, J. A.-U. Uribe, J. Y. W. A.-Y. Wang, Y. L. A.-Y. Liu, T. X. A.-T. Xing, and H. A.-B. H. Baghaei, "Design of an inexpensive high-sensitivity rodent-research PET camera (RRPET)," in *Proc. IEEE Nuclear Science Symp. Conf. Rec.*, 2003, pp. 2058–2062.
- [17] H. Baghaei, Y. Zhang, H. Li, Y. Wang, S. Kim, R. A. Ramirez, J. Liu, S. Liu, and W.-H. Wong, "GATE Monte Carlo simulation of a high-sensitivity and high-resolution LSO-based small animal PET camera," *IEEE Trans. Nucl. Sci.*, vol. 54, pp. 1568–1573, 2007.
- [18] L. R. MacDonald, K. Iwata, B. E. Patt, J. S. Iwanczyk, A. B. Hwang, M. C. Wu, and B. H. Hasegawa, "Evaluation of x-ray detectors for dual-modality CT-SPECT animal imaging," *Proc. SPIE*, vol. 4786, pp. 91–102, 2002.

- [19] K. B. Parnham, S. Chowdhury, J. Li, D. J. Wagenaar, and B. E. Patt, "Second-generation, tri-modality pre-clinical imaging system," in *Proc. IEEE Nuclear Science Symp. Conf. Rec.*, 2006, pp. 1802–1805.
- [20] R. Siddon, "Fast calculation of the exact radiological path for 3-D CT," *Med. Phys.*, vol. 12, pp. 252–255, 1985.
- [21] M. J. Berger, J. H. Hubbell, S. M. Seltzer, J. Chang, J. S. Coursey, R. Sukumar, and D. S. Zucker, XCOM: Photon Cross Sections Database, NBSIR 87-3597, Gaithersburg, MD, Ionizing Radiation Division, Physics Laboratory, National Institute of Standards and Technology [Online]. Available: <http://physics.nist.gov/PhysRefData/Xcom/Text/XCOM.html>
- [22] *National Electrical Manufacturers Association, NEMA Standards Publication NU 4- 2008. Performance Measurements of Small Animal Positron Emission Tomographs*. Rosslyn, VA: National Electrical Manufacturers Assoc., 2008.
- [23] A. M. Loening and S. S. Gambhir, "AMIDE: A free software tool for multimodality medical image analysis," *Mol. Imag.*, vol. 2, pp. 131–137, Jul. 2003.
- [24] H. Zaidi and B. H. Hasegawa, "Determination of the attenuation map in emission tomography," *J. Nucl. Med.*, vol. 44, pp. 291–315, 2003.
- [25] A. Bockisch, T. Beyer, G. Antoch, L. S. Freudenberg, H. Kuhl, J. F. Debatin, and S. P. Muller, "Positron emission tomography/computed tomography-imaging protocols, artifacts, and pitfalls," *Mol. Imag. Biol.*, vol. 6, pp. 188–199, 2004.
- [26] M. Ay and H. Zaidi, "Assessment of errors caused by x-ray scatter and use of contrast medium when using CT-based attenuation correction in PET," *Eur. J. Nucl. Med. Mol. Imag.*, vol. 33, pp. 1301–1313, 2006.